

Effect of IMF B_y on the Entry of Solar Wind Ions Into the Near-Earth Tail Lobe: Global Hybrid Simulation and MMS Observation

Chih-Ping Wang¹ , Xiaoyan Xing² , Xueyi Wang³ , Levon A. Avanov⁴ , Yu Lin³ , Robert J. Strangeway⁵ , and H. Y. Wei⁵ 

¹Department of Atmospheric and Oceanic Sciences, University of California, Los Angeles, CA, USA, ²XS Research LLC, Wilmette, IL, USA, ³Physics Department, Auburn University, Auburn, AL, USA, ⁴Goddard Space Flight Center, NASA, Greenbelt, MD, USA, ⁵Department of Earth, Planetary, and Space Physics, University of California, Los Angeles, CA, USA

Key Points:

- Global hybrid simulations predict that the low-latitude mantle plasma can form in the near-Earth lobe controlled by interplanetary magnetic field (IMF) B_y .
- Low-latitude mantle is in dawnside northern lobe and duskside southern lobe for positive IMF B_y . The asymmetry reverses for negative IMF B_y .
- Statistical analysis of magnetospheric multiscale data supports the simulation predicted dependence of near-Earth low-latitude mantle on the IMF B_y direction

Supporting Information:

Supporting Information may be found in the online version of this article.

Correspondence to:

C.-P. Wang,
cat@atmos.ucla.edu

Citation:

Wang, C.-P., Xing, X., Wang, X., Avanov, L. A., Lin, Y., Strangeway, R. J., & Wei, H. Y. (2022). Effect of IMF B_y on the entry of solar wind ions into the near-Earth tail lobe: Global hybrid simulation and MMS observation. *Journal of Geophysical Research: Space Physics*, 127, e2022JA030800. <https://doi.org/10.1029/2022JA030800>

Received 29 JUN 2022
Accepted 11 AUG 2022

Abstract Global simulations predict that the low-latitude mantle may be an important pathway for the solar wind entry into the tail magnetosphere close to the current sheet when interplanetary magnetic field (IMF) B_y dominates over IMF B_z . To evaluate this entry mechanism in the near-Earth tail ($X \sim -10$ – $-20 R_E$), we investigate the predictions from 3D global hybrid simulations as well as in situ observations by magnetospheric multiscale (MMS) spacecraft. The simulations predict that the low-latitude mantle plasma can appear in the near-Earth tail lobe extending inward approximately $5 R_E$ from the flank magnetopause. The low-latitude mantle plasma appears in the dawnside northern lobe and duskside southern lobe during positive IMF B_y , while the opposite asymmetry is seen during negative IMF B_y . After a change in the IMF B_y direction arriving at the bow shock nose, it takes another ~ 15 – 30 min for the asymmetry to completely reverse to the opposite sense in the near-Earth tail. We present six MMS events in the tail lobe showing that the existence and absence of the low-latitude mantle plasma is consistent with the predicted asymmetries. Statistical analysis of 5 years of MMS observations shows that the dependencies of the magnitudes of the lobe densities and tailward field-aligned flow speeds on the IMF B_y directions are consistent with the predicted contributions from the low-latitude mantle plasma in the expected lobe regions.

1. Introduction

Plasma from the solar wind and ionosphere are the two major particle sources for the Earth's magnetosphere. The entry of the solar wind particles into the magnetosphere and their subsequent transport within the magnetosphere is crucial to the formation and dynamics of the plasma sheet. There are several solar wind entry mechanisms and routes depending on the interplanetary magnetic field (IMF) orientations (Wing et al., 2014). When IMF is northward, the solar wind plasma entry into the plasma sheet can occur along the flanks through processes including Kelvin-Helmholtz instability (e.g., Nykyri & Otto, 2001; Otto & Fairfield, 2000) or wave diffusion (e.g., Chaston et al., 2008; Johnson & Cheng, 1997), or the entry occurs through high-latitude double cusp reconnection (e.g., Crooker, 1992; Li et al., 2005, 2009; Raeder et al., 1995). When IMF is southward, the solar wind plasma first enters the high-latitude tail lobes through the cusp and forms high-latitude mantle plasma (e.g., Trainer et al., 2021), then these high-latitude mantle particles $E \times B$ drift toward the current sheet and enter the tail plasma sheet (e.g., Ashour-Abdalla et al., 1993). Furthermore, when IMF B_y component becomes more substantial relative to IMF B_z , simulations and theories (e.g., Grzedzielski & Macek, 1988; Pilipp & Morfill, 1978; Sibeck & Lin, 2014; Siscoe & Sanchez, 1987) predicted that the solar wind particles can enter the tail lobe at low-latitudes through the open flank magnetopause and forms the low-latitude mantle. The resulting low-latitude mantle plasma is magnetosheath-like plasma in the magnetosphere flowing tailward along the open magnetic field lines but with reduced density and tailward speed than the adjacent magnetosheath. Compared to the high-latitude mantle formed by plasma coming from the cusp, the low-latitude mantle plasma is considerably denser (e.g., Pilipp & Morfill, 1978) and closer to the current sheet, and is asymmetric between the northern and southern lobes depending on the IMF B_y direction. As illustrated in Figure 1 based on the global magnetohydrodynamics (MHD) simulations for different IMF B_y directions (e.g., Wang et al., 2014), when IMF B_y is positive (Figure 1a), the low-latitude mantle is formed in the southern (northern) lobe on the duskside (dawnside), the asymmetry switches to the opposite sense when IMF B_y is negative (Figure 1b). The above predictions of the low-latitude mantle have been evaluated with satellite observations (e.g., Gosling et al., 1984, 1985; Haerendel

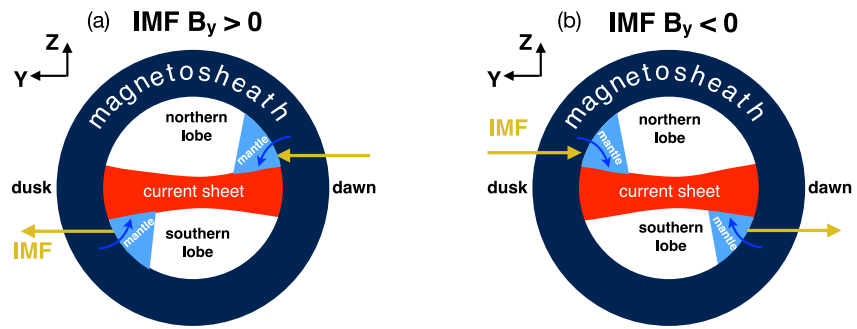


Figure 1. Schematic illustration of the region of the low-latitude mantle in the nightside magnetosphere corresponding to (a) positive interplanetary magnetic field (IMF) B_y and (b) negative IMF B_y based on the simulation predictions.

& Paschmann, 1975; Hardy et al., 1975, 1976, 1979; Maezawa and Hori, 1998; Sicsoc et al., 1994; Taguchi et al., 2001; Wang & Xing, 2021; Wang et al., 2014). However, the majority of these previous global MHD simulations and observational studies mainly investigated the mid-tail and distant-tail regions beyond $X \sim -20 R_E$. To our knowledge, there has been only one observational study showing one single event for the low-latitude mantle in the near-Earth tail at $X \sim -12 R_E$ (Taguchi et al., 2001). Depending on the IMF directions, the shocked solar wind in the magnetosheath can exhibit dawn-dusk asymmetries in several plasma and magnetic field parameters, which can be attributed to processes in either MHD or kinetic scales (e.g., Dimmock et al., 2017). It remains to be investigated whether dawn-dusk asymmetric magnetosheath conditions resulting from ion kinetic processes could affect the magnetopause reconnection in a way that can result in low-latitude mantle appearance different from the MHD predictions shown in Figure 1. Therefore, the objective of this study is to use global 3D hybrid simulations to investigate the low-latitude mantle in the near-Earth tail lobe ($X \sim -10$ – $-20 R_E$) and use the observations of magnetospheric multiscale (MMS) spacecraft to statistically evaluate the dependences on the IMF B_y directions predicted by the simulations. This paper is organized as follows. The hybrid simulation predictions of the spatial distributions and evolution of the low-latitude mantle in the near-Earth tail are presented in Section 2. In Section 3, we describe the MMS and IMF data and present six MMS events and statistical analysis results. Summary and discussion are given in Section 4.

2. Global Hybrid Simulation

Depending on the IMF B_y orientation, the quasi-parallel bow shock can shift to either the dawnside or duskside. The different ion kinetic dynamics in the quasi-parallel and quasi-perpendicular bow shock, for example, the ion foreshock is formed primarily in front of the quasi-parallel bow shock, thus introduces dawn-dusk magnetosheath asymmetries that are different from the asymmetries due to MHD processes. It has not been investigated whether the MHD predicted asymmetries of the low-latitude mantle plasma illustrated in Figure 1 still persist when the dawn-dusk asymmetries due to ion kinetic effects are taken into account. Therefore, here we present the results from a global 3D hybrid simulation using the AuburnN Global hybrid Code in 3D (ANGIE3D) hybrid code (Lin et al., 2014). The ANGIE3D code has been used in simulations of the solar wind-magnetosphere coupling and global dynamics in the magnetosphere, including the magnetotail, magnetopause, and plasma sheet (Lin et al., 2014, 2017, 2021, 2022; Lu et al., 2016; Lu, Lin, et al., 2015; Lu, Lu, et al., 2015; Wang et al., 2020, 2021).

2.1. Simulation Setups

In the ANGIE3D code, the ions (H^+ , He^+ , O^+) are treated as discrete, fully kinetic particles, and the electrons are treated as a massless fluid. Quasi charge neutrality is assumed. Detailed descriptions of the equations for ion particle motion, electric and magnetic fields, and assumptions used in the ANGIE3D code are given in Lin et al. (2014). The code is valid for low-frequency physics with $\omega \sim \Omega_i$ and $k\rho_i \sim 1$ (wavelength $\lambda \sim 6\rho_i$), where ω is the wave frequency, k is the wave number, Ω_i is the ion gyrofrequency, and ρ_i is the ion Larmor radius. An inner boundary is assumed at the geocentric distance of $r \approx 3 R_E$. For the region of the inner magnetosphere, a cold, incompressible ion fluid is assumed to be dominant for $r < 6 R_E$, which coexists with particle ions, since this simulation focuses on the dynamics and ion kinetic physics in the tail magnetosphere. The inclusion of the

cold ion fluid in the inner magnetosphere simplifies the conditions for the fluid-dominant low-altitude, inner boundary. A combination of spherical and Cartesian coordinates is used at the inner boundary. The loss cone effect at the inner boundary is considered, with the particles outside of the loss cone at $r = 3 R_E$ being reflected, while those within the loss cone being removed from the simulation domain. The \mathbf{E} and \mathbf{B} fields at the boundary reside on the Cartesian boundary approximating the spherical boundary, which are extrapolated to an extra grid point inside the $r = 3 R_E$ surface. The \mathbf{B} field is assumed to maintain the dipole field values at the inner boundary. The ionospheric conditions (1,000 km altitude) are incorporated into the ANGIE3d code. The FACs, calculated within the inner boundary, are mapped along the geomagnetic field lines into the ionosphere as input to compute ionospheric potential.

For the simulations presented here, only H^+ ions are modeled. The simulation domain is $20 \geq X \geq -60$, $32 \geq Y \geq -32$, $32 \geq Z \geq -32 R_E$ in the geocentric solar magnetospheric (GSM) coordinates. To accomplish this large-scale simulation with the available computing resources and still produce physical results, we choose the solar wind d_i to be $0.1 R_E$ (about six times larger than the realistic value) and the cell dimensions to be $n_x \times n_y \times n_z = 502 \times 507 \times 400$. Also, we use time-independent nonuniform cell sizes (ranging from ~ 0.1 to $0.5 R_E$) so that we can appropriately assign cell sizes comparable to the d_i values in different key regions from the solar wind to the outer magnetosphere. The bow shock and magnetopause form self-consistently by the interaction of the solar wind with the geomagnetic dipole. Simplified ionospheric conductance with uniform Pederson conductance of 10 S and Hall conductance of 5 S is specified.

We use the results from the ANGIE3D simulation runs that had been conducted previously for other investigations (some of the simulations have been published, e.g., Wang et al. (2020, 2021)). These simulations all have non-zero IMF B_y and magnitudes of the IMF components and solar wind parameters specified in these simulations are all within observed ranges, but they can be very different from one simulation to another, such as very different solar wind speeds, because they were designed for different focus targets. Nevertheless, we found that the IMF B_y dependence of the appearance of the low-latitude mantle plasma, as shown later in Section 2.2, is qualitatively similar in these simulations. Hence, we choose two of the simulation runs to present, run 1 is with steady IMF B_y condition to show the general features of the low-latitude mantle in the tail, and run 2 is with IMF B_y changing direction to show the time scale for the tail low-latitude mantle to appear after the IMF B_y change. The conditions for the two runs are the following: (a) Run 1 is for steady IMF B_y with time-independent IMF and solar wind conditions: The IMF condition is (3, -2, 0) nT, representing a typical Parker spiral, the solar wind density is 6 cm^{-3} , the isotropic solar wind ion temperature is 10 eV, and the solar wind velocities are (-320, 0, 0) km/s. These IMF and solar wind values are within the typically observed ranges. (b) Run 2 is for the IMF B_y changing directions with time-independent solar wind conditions: The step-change in the IMF direction from (0, -8, 0) to (0, 8, 0) nT is specified by an IMF discontinuity plane with a half-thickness of $0.3 R_E$ and the normal of (1, 0, 0) (the IMF B_y temporal variation at a fixed location in front of the bow shock can be seen later in Figure 4d). The solar wind density is 6 cm^{-3} , the isotropic solar wind ion temperature is 10 eV, and the solar wind velocities are (-700, 0, 0) km/s. These IMF and solar wind values are higher than those used in run 1 and they may be observed during high-speed solar wind streams.

2.2. Hybrid Simulation Results

2.2.1. Spatial Distributions of Low-Latitude Mantle and Asymmetries

To show the spatial distributions of the low-latitude mantle, we present in Figures 2 and 3 the simulation results from run 1 at $t = 94$ min when the near-Earth magnetotail has been relatively steady under the constant IMF and solar wind conditions. Figure 2a shows the simulated Y-Z distributions for B_x , ion density (N_i), and ion bulk flow speed in the $-X$ direction ($-V_x$) at $X = -15 R_E$. As indicated by the ions with substantial densities and tailward field-aligned flow (approximately enclosed by the magenta dotted circles in the N_i and $-V_x$ plots), the low-latitude mantle ions appear in the duskside northern lobe and dawnside southern lobe, consistent with Figure 1a. Figure 2b shows the X-Y distributions of the regions of the solar wind, the magnetosheath, and the magnetosphere at $Z = -8 R_E$ (this Z value is chosen to cut across the dawnside low-latitude mantle ions in the southern lobe). The foreshock is upstream of the dawnside bow shock. There are clear dawn-dusk asymmetries seen in the magnetosheath magnetic fields, densities, and flow speeds. Nevertheless, these magnetosheath asymmetries, with ion kinetic effects included, do not appear to qualitatively alter the expected dawn-dusk asymmetry of the low-latitude mantle shown in Figure 1 predicted by MHD. Figure 2c shows 3D views of N_i together with

ANGIE3D simulation run 1: IMF = (3, -2, 0) nT, $N_{sw} = 6 \text{ cm}^{-3}$, $V_{sw} = 320 \text{ km/s}$

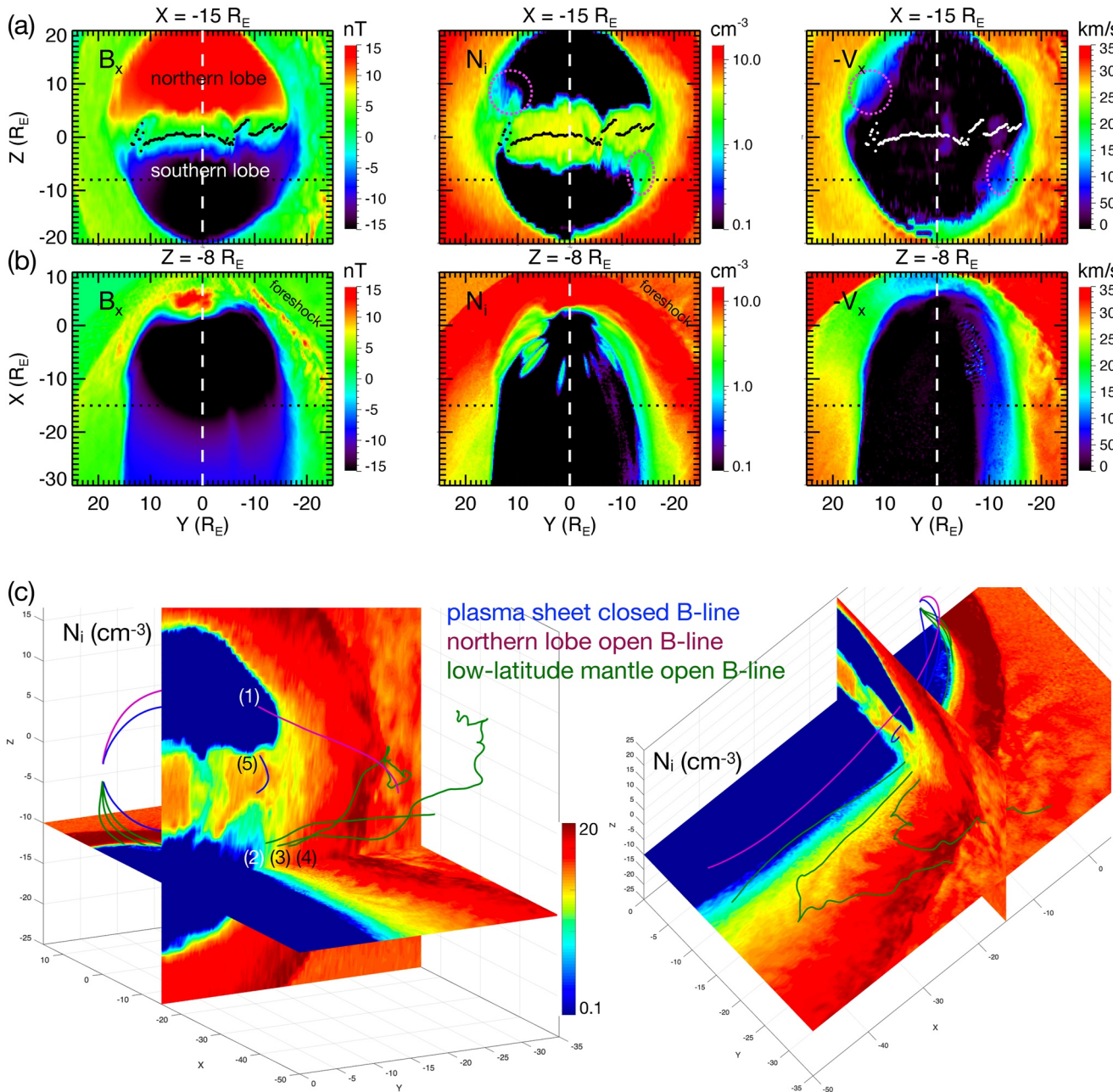


Figure 2. AuburnN Global hybrid CodE in 3D (ANGIE3D) simulation results from run 1 at $t = 94 \text{ min}$ (a) Y - Z distributions at $X = -15 R_E$ and (b) X - Y distributions at $Z = -8 R_E$ for B_x (left), N_i (center), and $-V_x$ (right). The white dashed line in (a and b) indicates $Y = 0$. The black or white dotted curve in (a) indicates the current sheet center. The low-latitude mantle plasma is indicated by the dotted magenta circle in the N_i and $-V_x$ plots in (a). (c) 3D views of N_i distributions with magnetic field lines crossing the five locations (1)–(5) at $X = -15 R_E$ in the northern lobe ((1), purple line), the southern low-latitude mantle ((2)–(4), green lines), and the plasma sheet ((5), blue line).

a few selected magnetic field lines threading through four locations in three different regions at $X = -15 R_E$: the purple line indicates an open field line in the northern lobe through location (1), the three green lines indicate three open field lines through locations (2)–(4) in the low-latitude mantle in the southern lobe, and the blue line indicates a closed field line through location (5) within the plasma sheet.

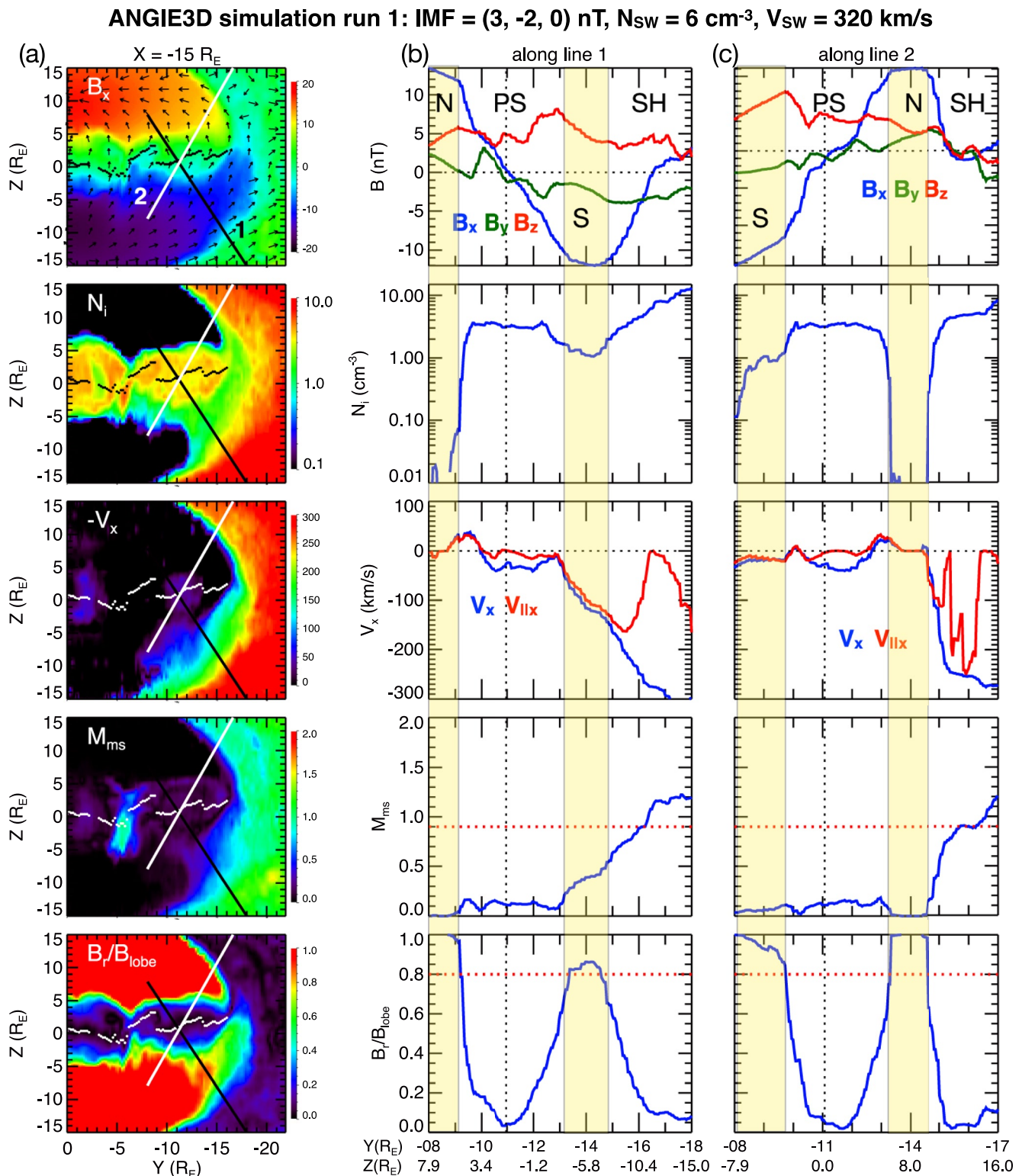


Figure 3. AuburnN Global hybrid CodE in 3D (ANGIE3D) simulation results from run 1 at $t = 94$ min at $X = -15 R_E$. (a) Top to bottom: The Y - Z distributions of B_x (the arrows indicate the directions of B_y - B_z), proton density (N_i), $-V_x$, magnetosonic Mach number (M_{ms}), and B_r/B_{lobe} . (b, c) Top to bottom: The profiles of magnetic field components, N_i , V_x and V_{llx} , M_{ms} and B_r/B_{lobe} along (b) line 1 and (c) line 2 indicated in (a). The yellow shaded regions indicate the lobe with “N” indicating northern lobe and “S” indicating southern lobe. The legend “SH” stands for the magnetosheath and “PS” for the plasma sheet.

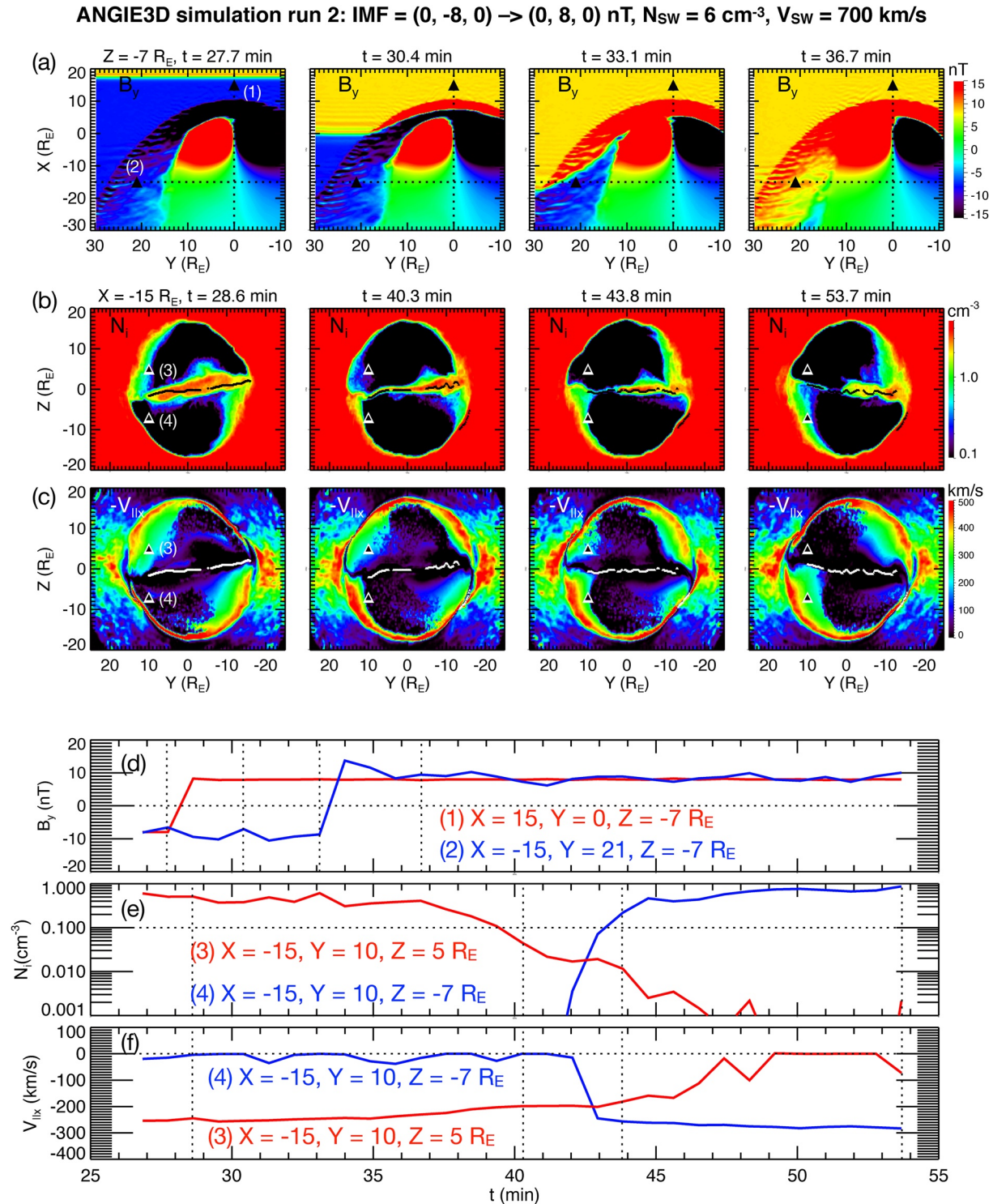


Figure 4. AuburnN Global hybrid CodE in 3D (ANGIE3D) simulation results from run 2. (a) X - Y distributions of B_y at $Z = -7 R_E$ at different times. Y - Z distributions of (b) N_i and (c) $-V_{lx}$ at $X = -15 R_E$ at different times. The black dotted curve in (b) and white dotted curve in (c) indicate the current sheet center. The temporal profiles of (d) B_y , (e) N_i , and (f) $-V_{lx}$ at the locations (1) and (2) indicated by triangles in (a) and locations (3) and (4) in (b) and (c).

We show in Figure 3 the plasma and magnetic field characteristics in different regions. Figure 3a shows the 2D spatial profiles in the Y - Z plane at $X = -15 R_E$ for B_x (with the directions of B_y - B_z indicated by the black arrows), N_i , $-V_x$, magnetosonic Mach number (M_{ms}), and B_r/B_{lobe} ratios in the dawnside magnetosphere and magnetosheath. The lobe magnetic field strength, B_{lobe} , is estimated from $B_{lobe} = (2\mu_0(P_{th} + P_{Br}))^{0.5}$, where P_{th} is

plasma thermal pressure (here we only consider ion thermal pressure), and P_{Br} is the magnetic field pressure of the radial magnetic field ($P_{Br} = B_r^2/(2\mu_0)$, $B_r^2 = B_x^2 + B_y^2$). For the estimation of B_{lobe} , we assume that the force balance in the Z -direction is assumed to be perpendicular to the current sheet plane) and that the curvature term associated with Bz can be neglected in this tail region (e.g., Xing et al., 2011). Figures 3b and 3c show the 1D profile along the lines 1 and 2 in Figure 3a, respectively. In order to show the plasma and magnetic field characteristics in different regions from the simulations and for the comparisons with the observations shown later in Section 3, each of the two straight lines is specifically chosen so that it cuts cross the regions of the lobe (yellow shaded regions with “N” and “S” indicating the northern and southern lobe, respectively), the plasma sheet (indicated by “PS” in the top plot), and the magnetosheath (indicated by “SH” in the top plot). Figures 3b and 3c show that M_{ms} is $>\sim 1$ in the magnetosheath and $<\sim 1$ inside the magnetosphere (including both the plasma sheet and lobe). The B_r/B_{lobe} ratio is high (~ 0.8 – 1) in the lobe and low (0 – ~ 0.8) in the plasma sheet. These ranges of M_{ms} and B_r/B_{lobe} for different regions are approximately consistent with the MMS observations that we will show later in Section 3. As shown in Figure 3b, compared to the absence of plasma in the northern lobe ($N_i < 0.1 \text{ cm}^{-3}$), the substantial density ($\sim 1 \text{ cm}^{-3}$) and tailward field-aligned flows ($|V_{lx}| \sim 100$ – 200 km/s , note that V_{lx} is the x -component of $V_{||}$ so field-aligned flow is tailward if V_{lx} is negative) seen in the southern lobe is contributed by the low-latitude plasma. Figures 3b and 3c show what a satellite would observe when crossing the flank magnetopause into the lobe with and without low-latitude mantle plasma, respectively. Observations for these two scenarios are presented in Sections 3.2 and 3.3.

2.2.2. Reverse of Low-Latitude Mantle Asymmetry After IMF By Direction Change

The IMF is rarely constant for an extended period time. To evaluate how quickly low-latitude mantle plasma can disappear or appear after a change in the IMF, in Figure 4 we present the results from run 2 with IMF B_y changing directions. Figure 4a shows the X-Y distributions of B_y at $Z = -7 R_E$ at different times from $t = 27$ – 37 min and Figure 4d shows the temporal profiles of B_y from $t = 25$ – 55 min at the two locations (1) and (2) (indicated by the two triangles in Figure 4a). The IMF discontinuity plane (IMF B_y is negative (positive) on the earthward (sunward) side of the plane) arrives at $X = 15 R_E$ in front of the bow shock nose (location (1)) at $t \sim 28 \text{ min}$ and in the tail magnetosheath at $X = -15 R_E$ (location (2)) at $t \sim 33 \text{ min}$. The propagation time from location (1) to (2) is $\sim 5 \text{ min}$, approximately consistent with the time needed for the solar wind to travel $30 R_E$ at a speed of 700 km/s . Figures 4b and 4c show the Y-Z distributions of N_i and $-V_{lx}$, respectively, at $X = -15 R_E$ at different times from $t = 28$ – 54 min , and Figures 4e and 4f show the temporal profiles of N_i and V_{lx} , respectively, from $t = 25$ – 55 min at the two locations (3) and (4) (indicated by the two triangles in Figures 4b and 4c). At $t = 28.6 \text{ min}$ when the magnetosphere is still affected by negative IMF B_y , the low-latitude plasma is seen at location 3 in the northern lobe but not at location 4 in the southern lobe. After the positive IMF B_y arrives at the tail magnetosheath at $t \sim 33 \text{ min}$, the density at location 3 starts to decrease at $t \sim 37 \text{ min}$ and it decreases quickly by an order of magnitude in 5 min (the tailward field-aligned speed also decrease but less quickly). On the other hand, densities and field-aligned flow speeds at location 4 start to increase quickly at $t \sim 42 \text{ min}$ and in $\sim 3 \text{ min}$ reaches the values similar to those seen at location 3 at $t = 28 \text{ min}$. Therefore, the north-south (or dawn-dusk) asymmetry of the low-latitude mantle at $X = -15 R_E$ completely reverses approximately 15 min after the arrival of the IMF direction change at the bow shock nose. This estimate is for a high-solar wind speed of 700 km/s . For the majority of the solar wind with speeds between ~ 350 and 450 km/s (shown later in Figure 8m), we expect that the flip would take approximately 30 min . This suggests that, for our evaluation of the correlation between the low-latitude mantle observed by MMS in the near-Earth tail lobe and the direction of the IMF B_y at the bow shock nose (propagated to the nose from the observed locations in the upstream solar wind), it is more appropriate to consider the history of the IMF directions in the past 30 min .

3. Observations

In this section, we present six MMS events in three pairs in Figures 5–7 to show the characteristics of lobe and low-latitude mantle under different IMF B_y directions. Each pair includes one event with the MMS in the duskside southern hemisphere and the other in the dawnside northern hemisphere. Both the first and second pairs were near the flank magnetopause with MMS crossing the magnetosheath and lobes with the first (second) pair during positive (negative) IMF B_y . The third pair was well within the magnetosphere with MMS crossing the lobe and

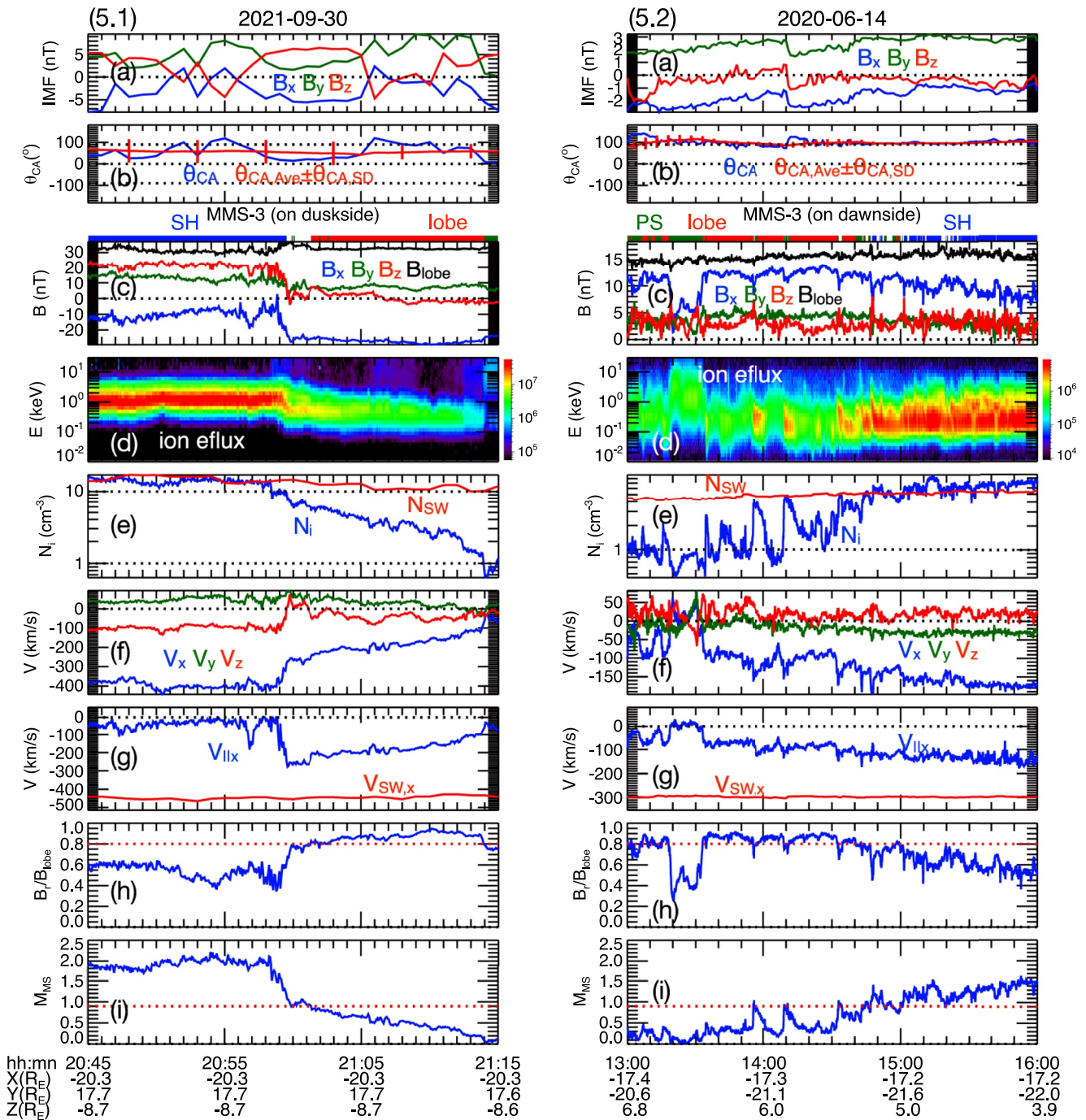


Figure 5. Two magnetospheric multiscale (MMS) magnetosheath-lobe crossing events observing low-latitude mantle during positive interplanetary magnetic field (IMF) B_y . The first event (5.1, left panels, 30 September 2021) was on the duskside and the second one (5.2, right panels, 14 June 2020) was on the dawnside. Temporal profiles of (a) interplanetary magnetic field and (b) θ_{CA} from OMNI, (c) MMS magnetic field, (d) MMS ion energy flux (the unit is $eV/(s\text{-sr}\text{-cm}^2\text{-eV})$), (e) MMS ion density (N_i) and the solar wind density (N_{sw}), (f) MMS ion bulk flow velocities, (g) MMS parallel flow in the x direction (V_{lx}) and solar wind $V_{sw,x}$, (i) B_r/B_{lobe} and (j) magnetosonic Mach number (M_{ms}). The X-Y locations are in geocentric solar magnetospheric coordinates. The intervals of magnetosheath (“SH” in blue), lobe (in red), and plasma sheet (“PS” in green) are indicated by the bars on the top of (c).

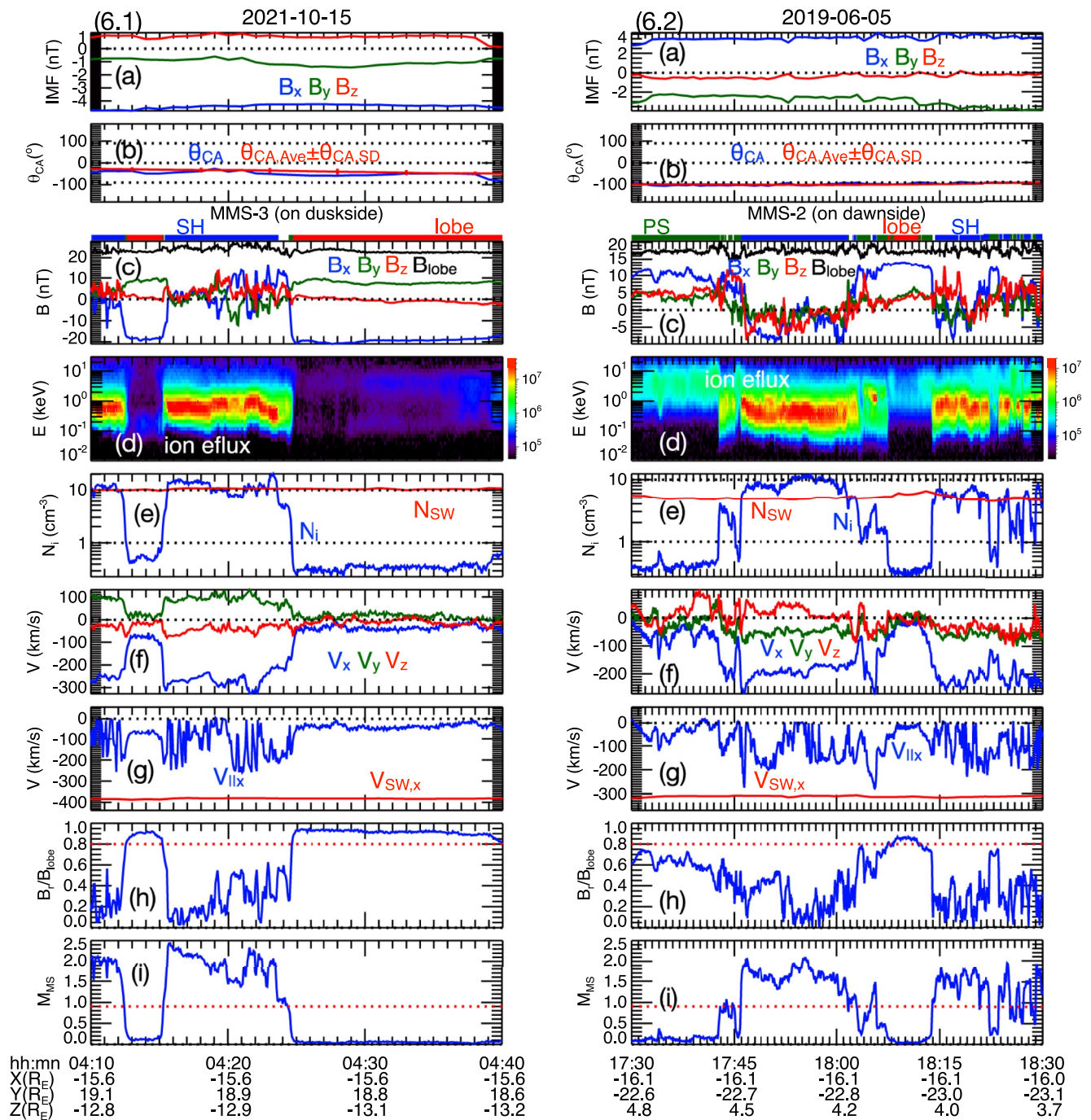


Figure 6. Two magnetospheric multiscale (MMS) magnetopause-lobe crossing events observing no low-latitude mantle during negative interplanetary magnetic field (IMF) B_y . The first event (6.1, left panels, 15 October 2021) was on the duskside and the second one (6.2, right panels, 5 June 2019) was on the dawnside. Temporal profiles of (a) interplanetary magnetic field and (b) θ_{CA} from OMNI, (c) MMS magnetic field, (d) MMS ion energy flux (the unit is $eV/(s\text{-sr}\text{-cm}^2\text{-eV})$), (e) MMS ion density (N_i) and the solar wind density (N_{sw}), (f) MMS ion bulk flow velocities, (g) MMS parallel flow in the x direction (V_{llx}) and solar wind $V_{sw,x}$, (i) B_l/B_{lobe} and (j) magnetosonic Mach number (M_{ms}). The X-Y locations are in geocentric solar magnetospheric coordinates. The intervals of magnetosheath (“SH” in blue), lobe (in red), and plasma sheet (“PS” in green) are indicated by the bars on the top of (c).

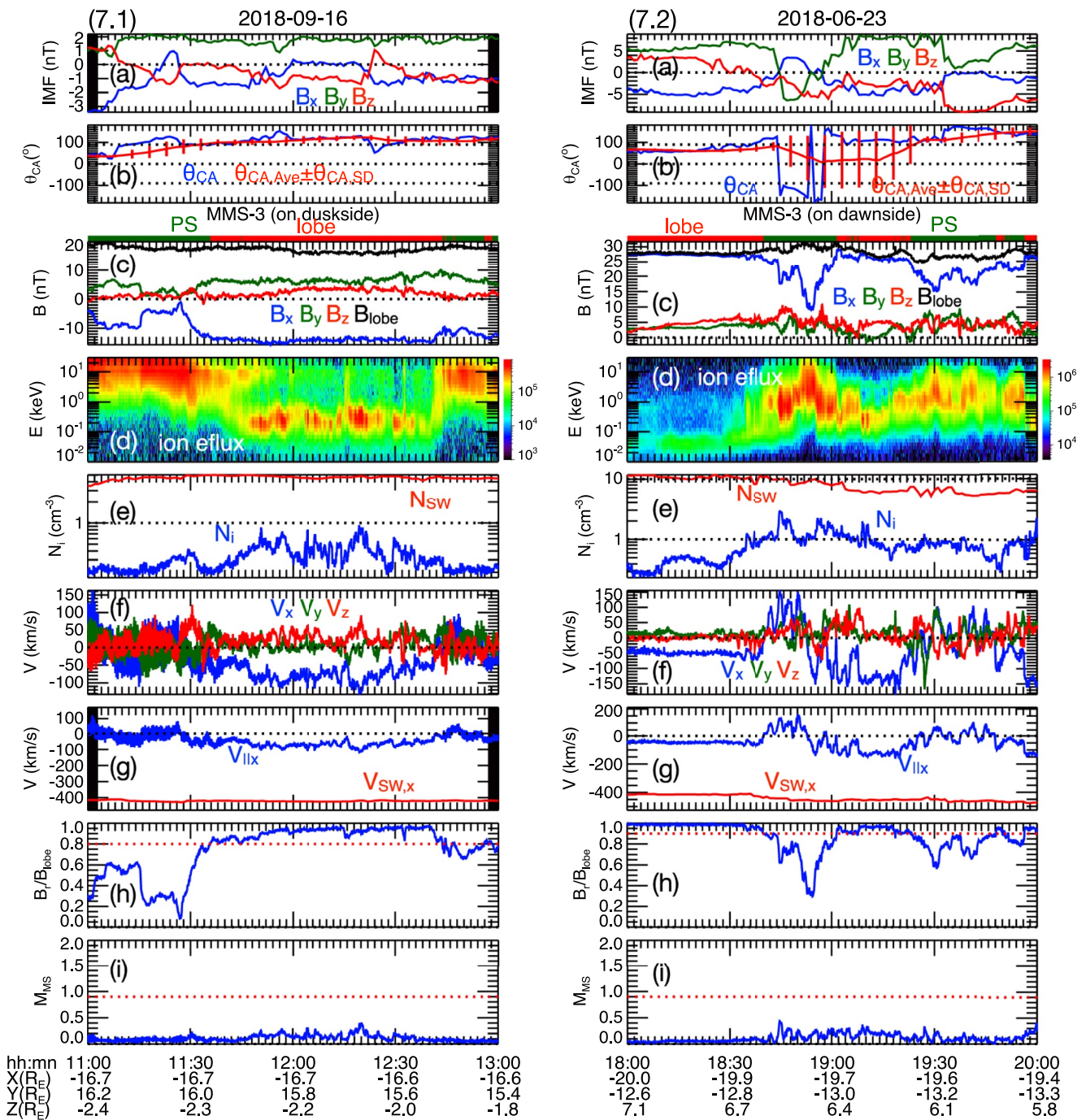


Figure 7. Two magnetospheric multiscale (MMS) lobe crossing events observing low-latitude mantle during positive interplanetary magnetic field (IMF) B_y . The first event (7.1, left panels, 16 September 2018) was on the duskside and the second one (7.2, right panels, 23 June 2018) was on the dawnside. Temporal profiles of (a) interplanetary magnetic field and (b) θ_{CA} from OMNI, (c) MMS magnetic field, (d) MMS ion energy flux (the unit is $eV/(s \cdot sr \cdot cm^2 \cdot eV)$), (e) MMS ion density (N_i) and the solar wind density (N_{SW}), (f) MMS ion bulk flow velocities, (g) MMS parallel flow in the x direction (V_{llx}) and solar wind $V_{sw,x}$, (i) B_l/B_{lobe} and (j) magnetosonic Mach number (M_{ms}). The X-Y locations are in geocentric solar magnetospheric coordinates. The intervals of magnetosheath (“SH” in blue), lobe (in red), and plasma sheet (“PS” in green) are indicated by the bars on the top of (c).

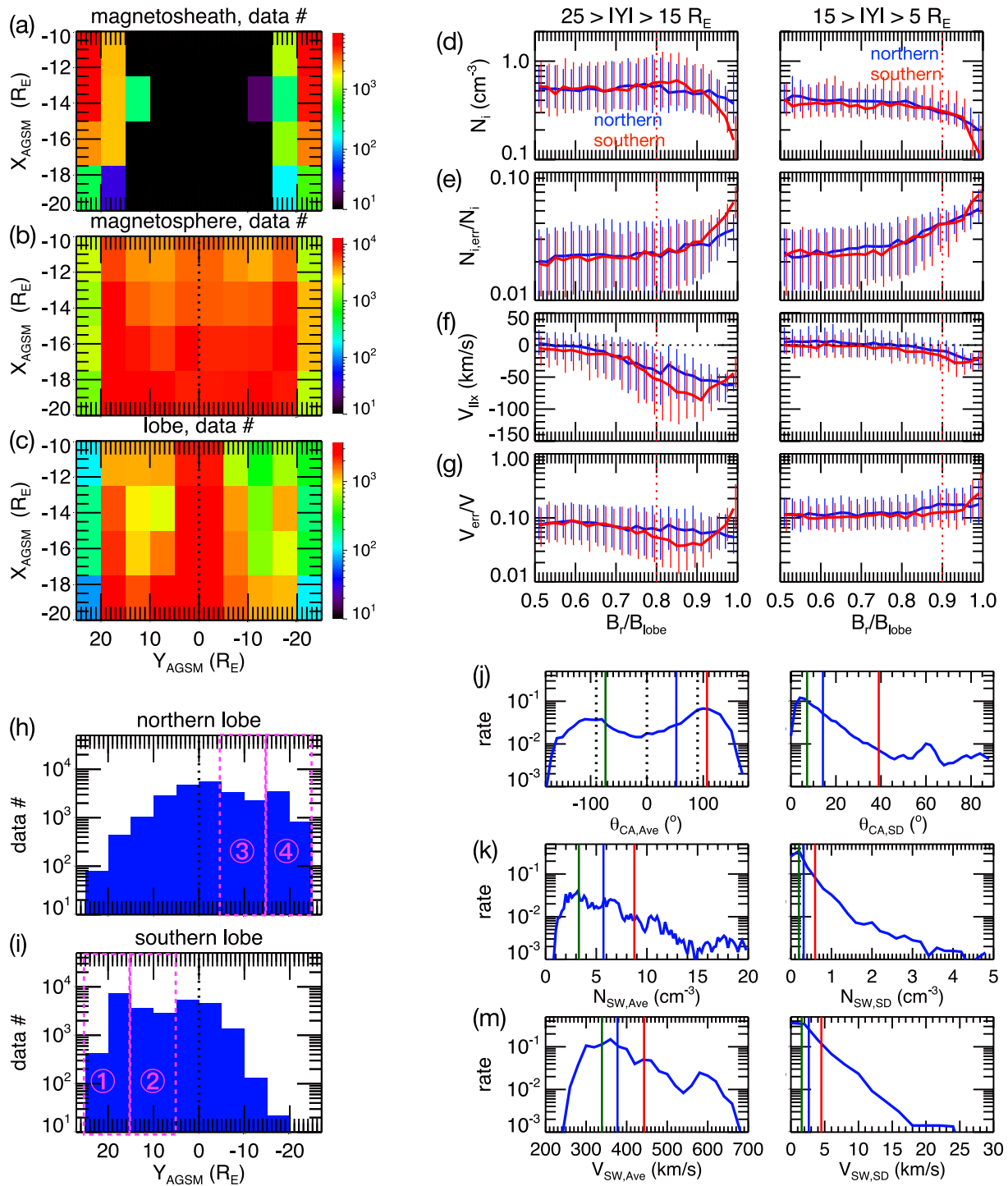


Figure 8. X - Y distributions of the numbers of data points for (a) the magnetosheath, (b) magnetosphere, and (c) lobe. The profiles of the medians (the vertical lines indicated the range of 25%–75% percentiles) of (d) N_i , (e) $N_{i, err}/N_i$ (f) V_{lx} , and (g) V_{err}/V as a function of B_r/B_{lobe} for the magnetospheric data in the northern (blue lines) and southern (red lines) hemisphere within $25 > |Y| > 15 R_E$ (left) and $15 > |Y| > 5 R_E$ (right). The numbers of data points in (h) northern lobe and (i) southern lobe (the data in the regions ① to ④ are analyzed in Figure 9). (j–m) The occurrence rates for the 30-min averages (left) and standard deviations (right) of (j) θ_{CA} , (k) N_{SW} , and (m) V_{SW} (the green, blue, and red vertical lines indicate 25%, 50%, and 75% percentiles, respectively) corresponding to the lobe data.

plasma sheet during positive IMF B_y . We choose these six events for relatively steady IMF B_y conditions during the period of interest.

3.1. MMS and IMF Data

In this study of the magnetotail, we use MMS observations from 2017 to 2021. MMS is a four-spacecraft constellation (Tooley et al., 2014). The spacecraft is at a low inclination orbit (28.5°) with an apogee of $\sim 25 R_E$ and an orbital period of ~ 3 days in 2017–2018 (the apogee was later raised to $\sim 29.3 R_E$ with an orbital period of 3.5 days). Every year, MMS observed the tail magnetosphere beyond $X = -10 R_E$ for around 6 months from May near the dawnside magnetopause to October near the duskside magnetopause. Ions from 10 eV to 30 keV (sample per 4.5 s) are measured by dual ion spectrometers (DIS) of fast plasma investigation (FPI; Pollock et al., 2016). In this study, we use the ion energy fluxes measured by FPI and the corresponding plasma moments, including ion densities, ion thermal pressures, ion bulk velocities, as well as the estimated errors for the measured density and velocity. The magnetic fields (16 samples/s) are measured by FIELDS instrument (Torbert et al., 2016). These data are from the fast survey mode observations.

For the IMF and solar wind conditions, including the solar wind density (N_{sw}), and the solar wind velocities (V_{sw}), we use the 1-min resolution OMNI data. The OMNI data have been propagated to the Earth's bow shock nose. Using the IMF components in geocentric solar magnetic (GSM) coordinates, we compute the IMF clock angle (θ_{CA}) between the IMF B_y and IMF B_z : $\theta_{CA} = \tan^{-1}(\text{IMF } B_y / \text{IMF } B_z)$. We define the range of θ_{CA} to be from -180° to 180° with 0° – 180° for IMF $B_y > 0$ and 0° – -180° for IMF $B_y < 0$, 0° for IMF $B_z > 0$ and IMF $B_y = 0$, $\pm 90^\circ$ for IMF $B_z = 0$, and $\pm 180^\circ$ for IMF $B_z < 0$ and IMF $B_y = 0$.

In this study, we use the MMS observations at $X = -10$ – $-20 R_E$. Since the OMNI data are at 1-min resolutions, we interpolate the MMS data to the OMNI data time frame. The OMNI data point at $t = t_0$ gives the IMF/solar wind conditions at the bow shock nose. As suggested from the simulation results shown in Figure 4, we consider the IMF and solar wind history during the past 30 min. We compute the averages and standard deviations of θ_{CA} , N_{sw} , and V_{sw} over a 30-min interval from $t_0 - 30$ min to t_0 . For the statistical analysis presented in Section 4, for each MMS data point at t_0 , we use $\theta_{CA,Ave}$, $\theta_{CA,SD}$, $N_{sw,Ave}$, $N_{sw,SD}$, $V_{sw,Ave}$, and $V_{sw,SD}$ as the corresponding IMF and solar wind conditions, where the subscript “Ave” stands for average and “SD” for standard deviation. Note that as mentioned later in Section 4 we also consider a longer history of the averages and standard deviations over a 60-min interval from $t_0 - 60$ min to t_0 to evaluate whether our choice of the IMF history affects the conclusions of the statistical analysis.

3.2. MMS Events

In this section, we present six MMS events in detail and compare the observations with the simulation predictions shown in Section 2.2. We first visually examined the time series of MMS magnetic fields and ion energy spectrum to approximately select the intervals when MMS was in the lobe tailward of $X = -10 R_E$ based on that magnetic field strength was dominated by $|B_x|$ and there was an absence of keV plasma sheet ions. We use the sign of B_x to determine that MMS was in the northern lobe ($B_x > 0$) or southern lobe ($B_x < 0$). We also determine the presence or absence of mantle plasma in the lobe. We then selected intervals of either magnetosheath-lobe crossing or lobe-plasma sheet crossing with the corresponding IMF B_y had remained mainly in one direction during the interval. Here we present six intervals that are suitable for comparing with the simulation results shown in Section 2.

3.2.1. Magnetosheath-Lobe Crossing Events During Positive IMF B_y

Figures 5.1 and 5.2 show two events with MMS crossing the lobe and magnetosheath near the duskside and dawnside flank magnetopause, respectively, during positive IMF B_y . Figure 5.1 shows the first event on 30 September 2021. During the event, IMF B_y was positive (Figure 5.1a) and θ_{CA} and $\theta_{CA,Ave}$ varied within the range of ~ 0 to 110° (Figure 5.1b, the $\theta_{CA,SD}$ is plotted every 5 min). The solar wind density (N_{sw}) was $> 10 \text{ cm}^{-3}$ (the red line in Figure 5.1e) and the solar wind speed in the x -direction ($V_{sw,x}$) was ~ 400 km/s (the red line in Figure 5.1g). Before $\sim 20:59$ UT, MMS was in the tail magnetosheath at $X \sim -20 R_E$ (indicated by the blue bar and the legend “SH” above Figure 5.1c) with ion densities (N_p , the blue line in Figure 5.1e) and ion bulk flow speed in the x -direction (V_x , the blue line in Figure 5.1f) close to the solar wind values, and with magnetosonic Mach number,

$M_{ms} > \sim 1$. Note that from investigating many magnetopause crossings observed by MMS beyond $X = -10 R_E$, in this study we define the region of $M_{ms} > 1.1$ as the magnetosheath and the region of $M_{ms} < 0.9$ as the magnetosphere, including the plasma sheet and the lobe. After $\sim 21:00$ UT, MMS entered the southern lobe (as indicated by the red bars and the legend “lobe” above Figure 5.1c), as indicated by B_x being negative (thus south of the tail current sheet). In the lobe region, the magnetic field was dominated by the B_x component (i.e., away from the current sheet center) with the absence of typical hot ($\sim \text{keV}$ and above) plasma sheet ions. Figure 5.1h shows that the B_y/B_{lobe} ratio in the lobe was $> \sim 0.8$. While in the lobe, MMS observed cold (a few hundreds of eV) magnetosheath-like ions (Figure 5.1d) flowing tailward along the magnetic field lines but with its densities ($\sim 1\text{--}7 \text{ cm}^{-3}$, the blue line in Figure 5.1e) and tailward field-aligned speeds ($V_{lx} \sim -100\text{--}200 \text{ km/s}$, the blue line in Figure 5.1g) substantially lower than the densities and speeds in the adjacent magnetosheath observed from 20:45 to 20:59 UT. This magnetosheath-like plasma is the low-latitude mantle plasma.

Figure 5.2 shows the second event on 14 June 2020 during a prolonged period of positive IMF B_y (Figures 5.2a and 5.2b). Before $\sim 14:10$ UT, MMS was within the dawnside tail magnetosphere at $X \sim -17 R_E$ and observed the regions of the lobe and the plasma sheet (the interval of the plasma sheet is indicated by the green bars and the legend “PS” above Figure 5.2c). Note that as shown later in Figures 8d–8g, for the data inside the magnetosphere ($M_{ms} < 0.9$), we define that MMS was in the lobe when $B_y/B_{lobe} > 0.9$ (0.8) in the region of $|Y| = [15, 25] R_E$ ($[5, 15] R_E$), otherwise MMS was in the plasma sheet. While in the northern lobe (B_x was positive as shown in Figure 5.2c), MMS observed the low-latitude mantle ions as indicated by their characteristics of the magnetosheath-like densities and tailward field-aligned flows with relatively lower values as compared to the magnetosheath values observed later after $\sim 14:40$ UT.

The above two events for positive IMF B_y conditions show the appearance of the low-latitude mantle in the duskside southern lobe (Figure 5.1) and in the dawnside northern lobe (Figure 5.2), which are consistent with the predictions illustrated in Figure 1a. The density and field-aligned flow characteristics of the low-latitude mantle plasma as compared to the magnetosheath plasma are qualitatively consistent with the hybrid simulation results shown in Figures 3a and 3b.

3.2.2. Magnetosheath-Lobe Crossing Events During Negative IMF B_y

Figures 6.1 and 6.2 show two events with MMS crossing the lobe and magnetosheath near the duskside and dawnside magnetopause, respectively, during negative IMF B_y . Figure 6.1 shows the first event on 15 October 2021. The IMF B_y had been steadily negative (Figures 6.1a and 6.1b). Figures 6.1c–6.1i show that MMS was first in the duskside tail magnetosheath at $X \sim -15 R_E$ and then entered the southern lobe after $\sim 04:25$ UT. While in the lobe, MMS did not observe low-latitude mantle plasma. Figure 6.2 shows the second event on 5 June 2019 during steady and negative IMF B_y (Figures 6.2a and 6.2b). Figures 6.2c–6.2i show that MMS was in the dawnside tail magnetosheath at $X \sim -16 R_E$. It entered briefly into the northern lobe between $\sim 18:09$ and $18:13$ UT but did not observe low-latitude mantle plasma.

The above two events show that, when IMF B_y was negative, MMS did not observe low-latitude mantle in the duskside southern lobe (Figure 4.1) and the dawnside northern lobe (Figure 4.2) just inside the magnetosheath, consistent with the predictions illustrated in Figure 1b. The observed plasma and magnetic profiles along the crossing from the magnetosheath to the lobe with the absence of the low-latitude mantle are qualitatively consistent with the hybrid simulation results shown in Figures 3a and 3c.

3.2.3. Lobe-Plasma Sheet Crossing Events During Positive IMF B_y

Figures 7.1 and 7.2 show two events with MMS within the magnetosphere crossing the lobe and plasma sheet near the duskside and dawnside, respectively, during positive IMF B_y . The MMS locations in these two events were deeper into the magnetosphere (i.e., farther away from the flank magnetopause), as compared to the four events shown in Figures 5 and 6. Figure 7.1 shows the first event on 16 September 2018. Figures 7.1c–7.1i show that MMS was in the duskside plasma sheet at $X \sim -16 R_E$ and $Y \sim 16 R_E$. It entered the southern lobe between 11:32 to 12:40 UT and observed the low-latitude mantle plasma. Figure 7.2 shows the second event on 23 June 2018. IMF B_y was mostly positive except for a brief (~ 10 min) excursion to negative values at $\sim 18:45$ UT (Figure 7.2a). The θ_{CA} became negative corresponding to the negative IMF B_y but $\theta_{CA, Ave}$ remained positive (Figure 7.2b). Figures 7.2c–7.2i show that MMS was in the dawnside magnetosphere at $X \sim -20 R_E$ and $Y \sim -13 R_E$. While MMS was in the northern lobe (as indicated by the red bars above Figure 7.2c), it observed the low-latitude mantle plasma.

The above two events show that, when IMF B_y was positive, MMS observed the low-latitude mantle in the dusk-side southern lobe (Figure 4.1) and the dawnside northern lobe (Figure 4.2), consistent with the predictions illustrated in Figure 1a. The transition from the plasma sheet plasma to the low-latitude mantle plasma is qualitatively consistent with the hybrid simulation results shown in Figures 3a and 3b.

3.3. MMS Statistical Results

3.3.1. Distributions of the Lobe and IMF Data

The MMS data from 2017 to 2021 are statistically analyzed. For the statistical study, aberrated GSM (AGSM) coordinates with 4° aberration angle are used for the MMS locations. Figures 8a and 8b show the X-Y spatial distributions of the numbers of the MMS data points (1-min resolutions) in the regions of the magnetosheath ($M_{ms} > 1.1$) and the magnetosphere ($M_{ms} < 0.9$), respectively. As shown in the simulation results presented in Section 2 and the observational events presented in Section 3, inside the magnetosphere, the B/B_{lobe} ratios are relatively lower in the plasma sheet region while relatively higher in the lobe region. However, there are no definite threshold values for the B/B_{lobe} ratios to separate the plasma sheet data from the lobe data. Figures 8d–8g show the quartiles of the magnetospheric N_i (Figure 8d), relative errors of ion density ($N_{i,ert}/N_i$, Figure 8e), V_{lx} (Figure 8f), and relative errors of ion bulk flow speed (V_{ert}/V , Figure 8g) as a function of B/B_{lobe} for the northern (red) and southern (blue) magnetosphere in the Y region closer to the magnetopause ($25 > |Y| > 15 R_E$, left panels) and deeper into the magnetosphere ($15 > |Y| > 5 R_E$, right panels). The densities drop quickly when the B/B_{lobe} ratios are higher than ~ 0.9 (Figure 7d). The tailward field-aligned flow speeds increase with increasing B/B_{lobe} and they increase quickly when the B/B_{lobe} ratios are higher than ~ 0.8 – 0.9 (Figure 8f). The relative errors shown in Figures 8e and 8g are generally higher in the region of higher B/B_{lobe} ratios, but they remain relatively small for both the density ($< \sim 0.1$, Figure 8e) and speed ($< \sim 0.2$, Figure 8g). Based on these statistical profiles, in this study we define the lobe region as $M_{ms} < 0.9$ and $B/B_{lobe} > \sim 0.8$ (0.9) in the region of $25 > |Y| > 15 R_E$ ($15 > |Y| > 5 R_E$). Note that as mentioned in Section 3.3.2 we also use stricter criteria for the lobe with higher B/B_{lobe} thresholds to evaluate whether the conclusions of our analysis are affected by the definition of the lobe. The X-Y spatial distributions of the available lobe data are shown in Figure 8c. Figures 8h and 8i show the numbers of the lobe data points as a function of Y in the northern lobe and southern lobe, respectively. The Y distributions show that the majority of the northern lobe data are available on the dawnside, while the majority of the southern lobe data are available on the duskside. This dawn-dusk asymmetry is due to the orbital bias.

Figures 8j, 8k, and 8m show the probability distributions (occurrence rates) of the 30-min averages (left) and standard deviations (right) of θ_{CA} , N_{sw} , and V_{sw} , respectively, for all the available lobe data points shown in Figures 8h and 8i. Figure 8j shows that, as indicated by the median $\theta_{CA,Ave}$ value shifting to $\sim 50^\circ$ (the blue vertical line), there were more lobe data points during positive IMF B_y than during negative IMF B_y . The distributions of $\theta_{CA,SD}$ indicate that the majority of the IMF conditions have θ_{CA} changes of less than $\sim 40^\circ$ within a 30 min interval (see the 75% quartile value as indicated by the red vertical line). Figure 8k shows that the majority of the $N_{sw,Ave}$ are within 4 – 10 cm^{-3} and the majority of $N_{sw,SD}$ are smaller than 1, which indicates that N_{sw} usually remains relatively constant within a 30 min interval. Similarly, the variations in the solar wind speed are usually very small on a time scale of 30 min, as indicated in Figure 8m that the magnitudes of $V_{sw,SD}$ ($< \sim 5 \text{ km/s}$) are much smaller than those of $V_{sw,Ave}$ (~ 350 – 450 km/s).

3.3.2. Dependence of Lobe Plasma on the IMF B_y Direction

As shown in Figures 8h and 8i, due to the orbital bias, the majority of the data for the northern (southern) lobe are on the dawnside (duskside), thus we select the data in four different lobe regions (as indicated by ①–④ in Figures 8h and 8i) to conduct statistical analysis: (1) Duskside southern lobe in $25 > Y > 15 R_E$; (2) Duskside southern lobe in $15 > Y > 5 R_E$; (3) Dawnside northern lobe in $-5 > Y > -15 R_E$; (4) Dawnside northern lobe in $-15 > Y > -25 R_E$. For each lobe region, we sort the MMS data into two groups, one for positive IMF B_y and one for negative IMF B_y direction using the following thresholds for $\theta_{CA,Ave}$ and $\theta_{CA,SD}$: (a) For positive IMF B_y and $|IMF B_y| > |IMF B_z|$: $45^\circ < \theta_{CA,Ave} < 35^\circ$ and $\theta_{CA,SD} < 40^\circ$. (b) For negative IMF B_y with $|IMF B_y| > |IMF B_z|$: $-45^\circ > \theta_{CA,Ave} > -135^\circ$ and $\theta_{CA,SD} < 40^\circ$. Note that the 75% percentile value of $\theta_{CA,SD}$ is $\sim 40^\circ$, as indicated by the red vertical line in Figure 8j. These ranges are chosen to inquire IMF B_y and B_z conditions in the past 30 min to have a dominant IMF B_y (i.e., $|IMF B_y| > |IMF B_z|$) and remain mostly in the same IMF B_y direction. Figure 9 shows the occurrence rates for $\theta_{CA,Ave}$ (Figure 9a), N_i (Figure 9c), $N_i/N_{sw,Ave}$ (Figure 9e), V_{lx} (Figure 9g), and

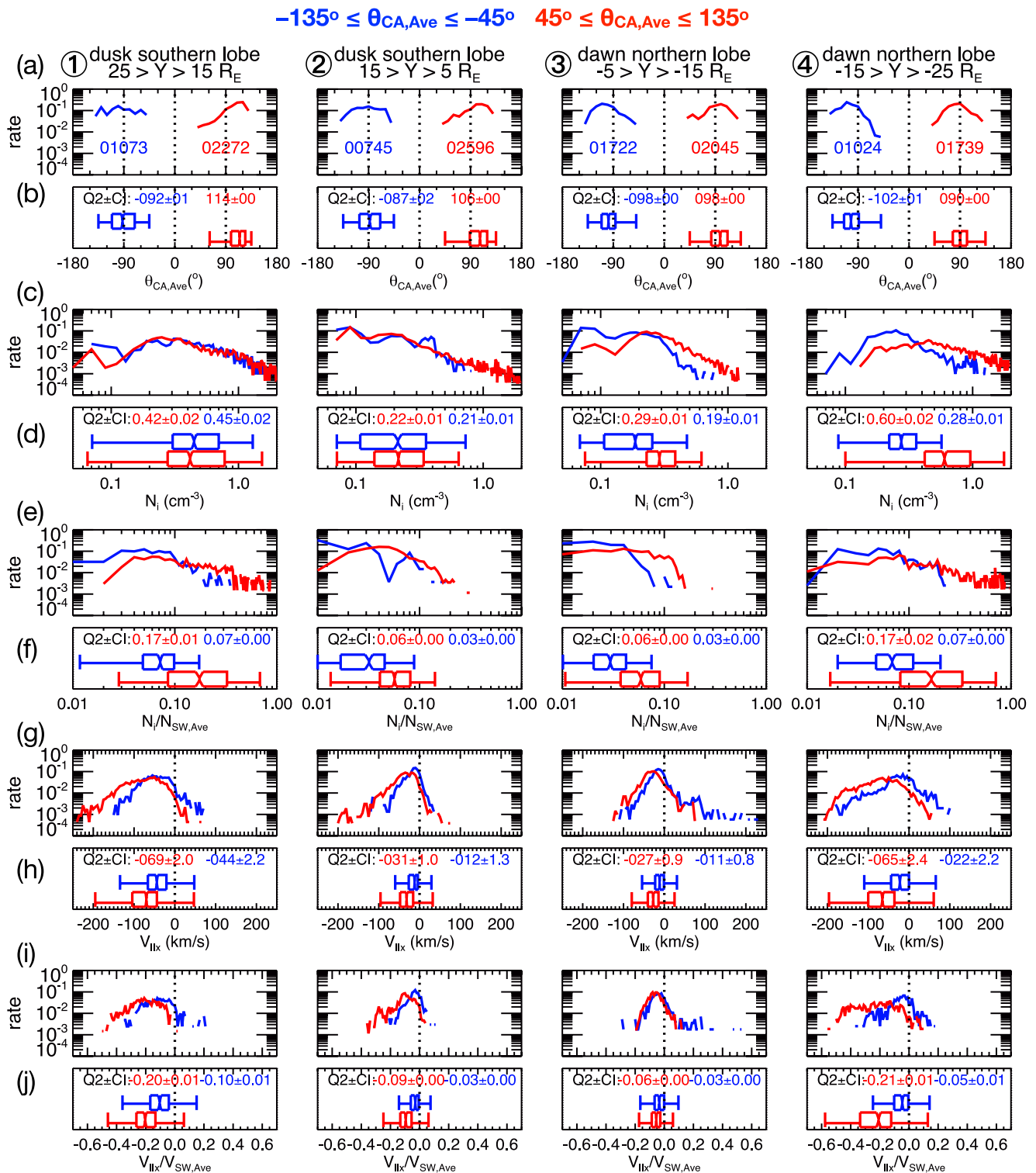


Figure 9. For the lobe data. The occurrence rates of (a) $\theta_{CA,Ave}$, (c) N_i , (e) $N_i/N_{SW,Ave}$, (g) V_{lik} , and (i) $V_{lik}/N_{SW,Ave}$ for $45^\circ \leq \theta_{CA,Ave} \leq 135^\circ$ (red) and $-135^\circ \leq \theta_{CA,Ave} \leq -45^\circ$ (blue) in the four regions indicated in Figures 8h and 8i (the numbers of the data points used are indicated in (a)). Notched boxes of (b) $\theta_{CA,Ave}$, (d) N_i , (f) $N_i/N_{SW,Ave}$, (h) V_{lik} , and (j) $V_{lik}/N_{SW,Ave}$ for $45^\circ \leq \theta_{CA,Ave} \leq 135^\circ$ (red) and $-135^\circ \leq \theta_{CA,Ave} \leq -45^\circ$ (blue) (the Q2 and CI values are indicated in the plots).

$V_{lx}/V_{SW,Ave}$ (Figure 9i) in the four lobe regions for positive IMF B_y (red) and negative IMF B_y (blue). Here we present the results of $N_l/N_{SW,Ave}$ and $V_{lx}/V_{SW,Ave}$ considering that there should be positive correlations between the low-latitude mantle densities and the solar wind densities and between the mantle flow speeds and the solar wind speeds since the low-latitude mantle plasma results from the entry of the magnetosheath plasma through open flank magnetopause. Hence, by approximately removing the dependencies on the solar wind densities and solar wind speeds, the results of $N_l/N_{SW,Ave}$ and $V_{lx}/V_{SW,Ave}$ should better reveal the dependencies on IMF B_y than those of N_l and V_{lx} . We also show the notched boxplots with whiskers for $\theta_{CA,Ave}$ (Figure 9b), N_l (Figure 9d), $N_l/N_{SW,Ave}$ (Figure 9f), V_{lx} (Figure 9h), and $V_{lx}/V_{SW,Ave}$ (Figure 9j). Each notched box shows Q1 (25% percentile, the lower end of the box), Q2 (median, the line within the box), and Q3 (75% percentile, the upper end of the box) (also see Figure S1 in Supporting Information S1 for an illustrated explanation of the notched box and whiskers). The notch indicates a 95% confidence interval (CI) of the median. The CI is defined as $1.57 \cdot IQR/Num^{1/2}$, where IQR (inner quartile range) = $Q3 - Q1$ and Num is the number of the data points in each group (indicated in the occurrence rate plot in Figure 8a). The lower (upper) end of the notch is $Q2 - CI$ ($Q2 + CI$) with the values of Q2 and CI indicated in the plots. The lower (upper) whisker is $Q1 - 1.5 \cdot IQR$ ($Q3 + 1.5 \cdot IQR$). The range within the two whiskers should include 99.3% of the data if from a normal distribution.

As shown in Figure 9, the dependence of the lobe density and field-aligned tailward flow speeds on the IMF B_y direction is evident in the four lobe regions. The lobe densities are relatively higher and the field-aligned tailward flow speeds are higher during positive IMF B_y , as compared to those during negative IMF B_y . Comparing the notched boxes of the two groups indicates the statistical significance of the differences between the two groups. If the two boxes' notches do not overlap, then there is 95% confidence their medians differ. In the two lobe regions closer to the magnetopause (regions 1 and 4), the clear separation between the red and blue notches in all parameters (except for the N_l distributions in region 1) indicates that IMF B_y direction indeed effectively affects the lobe densities and field-aligned tailward flow speeds near the flank magnetopause. The dependencies on the IMF B_y are less significant deeper into the magnetosphere (regions 2 and 3). Note that we have also conducted the same analysis using higher B_l/B_{lobe} thresholds for the lobe data (Figure S2 in Supporting Information S1 shows the results using $B_l/B_{lobe} > \sim 0.85$ (0.95) in the region of $25 > |Y| > 15 R_E$ ($15 > |Y| > 5 R_E$) for the lobe) and considering longer IMF/solar wind history (Figure S3 in Supporting Information S1 shows the results using 60-min history, i.e., the averages and standard deviations within the interval of $(t_0 - 60 \text{ min}, t_0)$). The dependencies on the IMF B_y directions shown in Figures S2 and S3 in Supporting Information S1 are in principle the same as the results of Figure 9. These statistical results are consistent with the model predictions shown in Figures 1–4, supporting that the low-latitude mantle plasma can be formed in the near-Earth tail lobe $\sim 5\text{--}10 R_E$ inside the magnetopause resulting from the solar wind entry through open flank magnetopause during substantial IMF B_y .

4. Summary and Discussion

To understand the solar wind entry into the near-Earth tail affected by the IMF B_y directions, we investigated the simulation results from a global 3D hybrid model and the observational results from MMS. The key conclusions are the followings:

1. The simulations predict that the low-latitude mantle plasma, resulting from the entry of the solar wind plasma through the open flank magnetopause, can form in the near-Earth tail lobe. There is an asymmetry with the low-latitude mantle plasma appearing in the dawnside northern lobe and duskside southern lobe for positive IMF B_y . The opposite asymmetry is seen for negative IMF B_y . The asymmetries predicted by the hybrid simulations are qualitatively consistent with those by the MHD simulations.
2. The simulations show that after a step change in the IMF B_y direction arrives at the bow shock nose it takes another $\sim 15\text{--}30$ min for the asymmetries in the near-Earth tail to complete the reversal to the opposite sense. This time delay includes the time needed for the changed IMF B_y to propagate from the bow shock nose to the tail magnetosheath (depending on the solar wind speed) and newly open the magnetopause in the other hemisphere as well as the time needed for the magnetosheath ions entering from the new open magnetopause to convect into the tail lobe to form the low-latitude mantle (depending on the magnetospheric convection strength).
3. Statistical analysis of MMS observations shows that the magnitudes of the lobe densities and tailward field-aligned flow speeds depend on the IMF B_y directions with stronger dependencies seen in the lobe region closer to the flank magnetopause. The higher densities and stronger tailward field-aligned flow speeds during

a preferred IMF B_y direction are consistent with being attributed to the low-latitude mantle plasma as predicted by the simulations.

Wang et al. (2014, 2021) investigated the low-latitude mantle and the plasma sheet observed in the midtail around $X \sim -60 R_E$. They showed that low-latitude mantle plasma is often in direct contact with the plasma sheet, which allows the low-latitude mantle to be a more important pathway for the solar wind entry into the plasma sheet when the IMF B_y is dominant, as compared to other IMF conditions. As shown in Figure 7, such a direct contact of the low-latitude mantle with the plasma sheet is also observed in the near-Earth tail, suggesting that the low-latitude mantle can also be a pathway for the solar wind to enter the near-Earth plasma sheet. Further investigations with simulations and observations are needed in the future to better understand the importance of this pathway in the near-Earth tail.

Data Availability Statement

The simulation data can be found at <https://doi.org/10.6084/m9.figshare.20186828>. The MMS data are available for free via MMS Science Data Center (<https://lasp.colorado.edu/mms/sdc/public/about/how-to/>). The solar wind and IMF parameters are available for free at NASA CDAWeb (http://cdaweb.gsfc.nasa.gov/cdaweb/istp_public/).

References

- Ashour-Abdalla, M., Berchem, J. P., Büchner, J., & Zelenyi, L. M. (1993). Shaping of the magnetotail from the mantle: Global and local structuring. *Journal of Geophysical Research*, 98(A4), 5651–5676. <https://doi.org/10.1029/92JA01662>
- Chaston, C. C., Bonnell, J., McFadden, J. P., Carlson, C. W., Cully, C., Le Contel, O., et al. (2008). Turbulent heating and cross-field transport near the magnetopause from THEMIS. *Geophysical Research Letters*, 35(17), L17S08. <https://doi.org/10.1029/2008GL033601>
- Crooker, N. U. (1992). Reverse convection. *Journal of Geophysical Research*, 97(A12), 19363–19372. <https://doi.org/10.1029/92JA01532>
- Dimmock, A. P., Nykyri, K., Osmane, A., Karimabadi, H., & Pulkkinen, T. I. (2017). Dawn-dusk asymmetries of the Earth's dayside magnetosheath in the magnetosheath interplanetary medium reference frame. In S. Haaland, A. Runov, & C. Forsyth (Eds.), *Dawn-dusk asymmetries in planetary plasma environments*. <https://doi.org/10.1002/9781119216346>
- Gosling, J. T., Baker, D. N., Bame, S. J., Feldman, W. C., Zwickl, R. D., & Smith, E. J. (1985). North-south and dawn-dusk plasma asymmetries in the distant tail lobes: ISEE 3. *Journal of Geophysical Research*, 90(A7), 6354–6360. <https://doi.org/10.1029/JA090iA07p06354>
- Gosling, J. T., Baker, D. N., Bame, S. J., Hones, E. W., Jr., McComas, D. J., Zwickl, R. D., et al. (1984). Plasma entry into the distant tail lobes: ISEE-3. *Geophysical Research Letters*, 11(10), 1078–1081. <https://doi.org/10.1029/GL011i010p01078>
- Grzedzielski, S., & Macek, W. (1988). An open magnetopause model of the Earth's distant tail based on ISEE 3 evidence. *Journal of Geophysical Research*, 93(A3), 1795–1808. <https://doi.org/10.1029/JA093iA03p01795>
- Haerendel, G., & Paschmann, G. (1975). *Entry of solar wind plasma into the magnetosphere*. In B. Hultqvist & L. Stenflo (Eds.), *Physics of the hot plasma in the magnetosphere* (pp. 23–43).
- Hardy, D. A., Freeman, J. W., & Hills, H. K. (1976). *Plasma observations in the magnetotail*. In B. M. McCormac & D. Reidel (Ed.), *Magnetospheric particles and fields* (Vol. 89).
- Hardy, D. A., Hills, H. K., & Freeman, J. W. (1975). A new plasma regime in the distant geomagnetic tail. *Geophysical Research Letters*, 2(5), 169–172. <https://doi.org/10.1029/GL002i005p00169>
- Hardy, D. A., Hills, H. K., & Freeman, J. W. (1979). Occurrence of the lobe plasma at lunar distance. *Journal of Geophysical Research*, 84(A1), 72–78. <https://doi.org/10.1029/JA084iA01p00072>
- Johnson, J. R., & Cheng, C. Z. (1997). Kinetic Alfvén waves and plasma transport at the magnetopause. *Geophysical Research Letters*, 24(11), 1423–1426. <https://doi.org/10.1029/97GL01333>
- Li, W., Raeder, J., Dorelli, J., Øieroset, M., & Phan, T. D. (2005). Plasma sheet formation during long period of northward IMF. *Geophysical Research Letters*, 32(12), L12S08. <https://doi.org/10.1029/2004GL021524>
- Li, W., Raeder, J., Øieroset, M., & Phan, T. D. (2009). Cold dense magnetopause boundary layer under northward IMF: Results from THEMIS and MHD simulations. *Journal of Geophysical Research*, 114(A1), A00C15. <https://doi.org/10.1029/2008JA013497>
- Lin, Y., Wang, X., Sibeck, D. G., Wang, C.-P., & Lee, S.-H. (2022). Global asymmetries of hot flow anomalies. *Geophysical Research Letters*, 49(4), e2021GL096970. <https://doi.org/10.1029/2021GL096970>
- Lin, Y., Wang, X. Y., Fok, M.-C., Buzulukova, N., Perez, J. D., Cheng, L., & Chen, L.-J. (2021). Magnetotail-inner magnetosphere transport associated with fast flows based on combined global-hybrid and CIMI simulation. *Journal of Geophysical Research: Space Physics*, 126(3), e2020JA028405. <https://doi.org/10.1029/2020JA028405>
- Lin, Y., Wang, X. Y., Lu, S., Perez, J. D., & Lu, Q. (2014). Investigation of storm time magnetotail and ion injection using three-dimensional global hybrid simulation. *Journal of Geophysical Research: Space Physics*, 119(9), 7413–7432. <https://doi.org/10.1002/2014JA020005>
- Lin, Y., Wing, S., Johnson, J. R., Wang, X. Y., Perez, J. D., & Cheng, L. (2017). Formation and transport of entropy structures in the magnetotail simulated in a 3-d global hybrid code. *Geophysical Research Letters*, 44(12), 5892–5899. <https://doi.org/10.1002/2017GL073957>
- Lu, S., Lin, Y., Angelopoulos, V., Artemyev, A. V., Pritchett, P. L., Lu, Q., & Wang, X. Y. (2016). Hall effect control of magnetotail dawn-dusk asymmetry: A three-dimensional global hybrid simulation. *Journal of Geophysical Research: Space Physics*, 121(11), 11882–11895. <https://doi.org/10.1002/2016JA023325>
- Lu, S., Lin, Y., Lu, Q. M., Wang, X. Y., Wang, R. S., Huang, C., et al. (2015). Evolution of flux ropes in the magnetotail: A three-dimensional global hybrid simulation. *Physics of Plasmas*, 22(5), 052901. <https://doi.org/10.1063/1.4919615>
- Lu, S., Lu, Q., Lin, Y., Wang, X. Y., Ge, Y., Wang, R., et al. (2015). Dipolarization fronts as earthward propagating flux ropes: A three-dimensional global hybrid simulation. *Journal of Geophysical Research: Space Physics*, 120(8), 6286–6300. <https://doi.org/10.1002/2015JA021213>
- Maezawa, K., & Hori, T. (1998). The distant magnetotail: Its structure, IMF dependence, and thermal properties. (Eds.). In *New perspectives on the Earth's magnetotail*. In *Geophysical monograph series* (Vol. 105, pp. 1–20). American Geophys. Union.

Acknowledgments

C.-P. Wang is supported by NASA 80NSSC20K0714, 80NSSC22K1012, and AFOSR FY2–16 MURI. X. Xing is supported by NASA 80NSSC20K0714. X. Wang and Y. Lin are supported by NASA 80NSSC20K1322 and 80NSSC22K1012, and NSF EPSCoR grant OIA–1655280. L. Avanzo is supported by NASA Magnetospheric Multiscale mission. R. Strangeway is supported by NASA 80NSSC18K1220. H. Y. Wei is supported by UNH Subcontract #06-001. The authors thank J. H. King, N. Papatashvilli at AdnetSystems, NASA GSFC, and CDAWeb for providing the OMNI data.

- Nykyri, K., & Otto, A. (2001). Plasma transport at the magnetospheric boundary due to reconnection in Kelvin-Helmholtz vortices. *Geophysical Research Letters*, 28(18), 3565–3568. <https://doi.org/10.1029/2001GL013239>
- Otto, A., & Fairfield, D. H. (2000). Kelvin-Helmholtz instability at the magnetotail boundary: MHD simulation and comparison with geotail observations. *Journal of Geophysical Research*, 105(A9), 21175–21190. <https://doi.org/10.1029/1999JA000312>
- Pilipp, W. G., & Morfill, G. (1978). The formation of the plasma sheet resulting from plasma mantle dynamics. *Journal of Geophysical Research*, 83(A12), 5670–5678. <https://doi.org/10.1029/JA083iA12p05670>
- Pollock, C., Moore, T., Jacques, A., Burch, J., Gliese, U., Saito, Y., et al. (2016). Fast plasma investigation for magnetospheric multiscale. *Space Science Reviews*, 199(1–4), 331–406. <https://doi.org/10.1007/s11214-016-0245-4>
- Raeder, J., Walker, R. J., & Ashour-Abdalla, M. (1995). The structure of the distant geomagnetic tail during long periods of northward IMF. *Geophysical Research Letters*, 22(4), 349–352. <https://doi.org/10.1029/94gl03380>
- Sibeck, D. G., & Lin, R.-Q. (2014). Size and shape of the distant magnetotail. *Journal of Geophysical Research: Space Physics*, 119(2), 1028–1043. <https://doi.org/10.1002/2013JA019471>
- Siscoe, G. L., Frank, L. A., Ackerson, K. L., & Paterson, W. R. (1994). Properties of mantle-like magnetotail boundary layer: Geotail data compared with a mantle model. *Geophysical Research Letters*, 21(25), 2975–2978. <https://doi.org/10.1029/94gl01601>
- Siscoe, G. L., & Sanchez, E. (1987). An MHD model for the complete open magnetotail boundary. *Journal of Geophysical Research*, 92(A7), 7405–7412. <https://doi.org/10.1029/JA092iA07p07405>
- Taguchi, S., Kishida, H., Mukai, T., & Saito, Y. (2001). Low-latitude plasma mantle in the near-Earth magnetosphere: Geotail observations. *Journal of Geophysical Research*, 106(A2), 1949–1954. <https://doi.org/10.1029/2000ja900100>
- Tooley, C. R., Black, R. K., Robertson, B. P., Stone, J. M., Pope, S. E., & Davis, G. T. (2014). The magnetospheric multiscale constellation. *Space Science Reviews*, 199(1–4), 23–76. <https://doi.org/10.1007/s11214-015-0220-5>
- Torbert, R. B., Russell, C. T., Magnes, W., Ergun, R. E., Lindqvist, P.-A., LeContel, O., et al. (2016). The FIELDS instrument suite on MMS: Scientific objectives, measurements, and data products. *Space Science Reviews*, 199(1–4), 105–135. <https://doi.org/10.1007/s11214-014-0109-8>
- Trainer, K. J., Petrinec, S. M., & Fuselier, S. (2021). The location of magnetic reconnection at Earth's Magnetopause. *Space Science Reviews*, 217(3), 41. <https://doi.org/10.1007/s11214-021-00817-8>
- Wang, C.-P., Lyons, L. R., & Angelopoulos, V. (2014). Properties of low-latitude mantle plasma in the Earth's magnetotail: ARTEMIS observations and global MHD predictions. *Journal of Geophysical Research: Space Physics*, 119(9), 7264–7280. <https://doi.org/10.1002/2014JA020060>
- Wang, C.-P., Wang, X., Liu, T. Z., & Lin, Y. (2020). Evolution of a foreshock bubble in the midtail foreshock and impact on the magnetopause: 3-D global hybrid simulation. *Geophysical Research Letters*, 47(22), e2020GL089844. <https://doi.org/10.1029/2020GL089844>
- Wang, C.-P., Wang, X., Liu, T. Z., & Lin, Y. (2021). Impact of foreshock transients on the flank magnetopause and magnetosphere and the ionosphere. *Frontiers in Astronomy and Space Sciences*, 8, 160. <https://doi.org/10.3389/fspas.2021.751244>
- Wang, C.-P., & Xing, X. (2021). Solar wind entry into midtail current sheet via low-latitude mantle under dominant IMF B_y : ARTEMIS observation. *Journal of Geophysical Research: Space Physics*, 126(9), e2021JA029402. <https://doi.org/10.1029/2021JA029402>
- Wing, S., Johnson, J. R., Chaston, C. C., Echim, M., Escoubet, C. P., Lavraud, B., et al. (2014). Review of solar wind entry into and transport within the plasma sheet. *Space Science Reviews*, 184(1–4), 1–54. <https://doi.org/10.1007/s11214-014-0108-9>
- Xing, X., Lyons, L. R., Nishimura, Y., Angelopoulos, V., Donovan, E., Spanswick, E., et al. (2011). Near-Earth plasma sheet azimuthal pressure gradient and associated auroral development soon before substorm onset. *Journal of Geophysical Research*, 116(A7), A07204. <https://doi.org/10.1029/2011JA016539>